Catalysis Today 145 (2009) 227–235

Contents lists available at ScienceDirect

Catalysis Today

journal homepage: www.elsevier.com/locate/cattod

Structure and catalytic reactivity of Rh oxides

J. Gustafson [a,b], R. Westerström [a], A. Resta [a,c], A. Mikkelsen [a], J.N. Andersen [a], O. Balmes [c], X. Torrelles [d], M. Schmid [e], P. Varga [e], B. Hammer [f], G. Kresse [g], C.J. Baddeley [b], E. Lundgren [a,*]

[a] Department of Synchrotron Radiation Research, Institute of Physics, Lund University, Box 118, S-221 00 Lund, Sweden
[b] EASTChem School of Chemistry, University of St Andrews, St Andrews, KY16 9ST, UK
[c] ESRF, 6 rue Jules Horowitz, F-38043 Grenoble Cedex, France
[d] Institut the Ciencia de Materials de Barcelona (C.S.I.C.), 08193 Bellaterra, Barcelona, Spain
[e] Institut für Allgemeine Physik, Technische Universität Wien, A-1040 Wien, Austria
[f] Interdisciplinary Nanoscience Center (iNANO) and Department of Physics and Astronomy, University of Aarhus, DK-8000 Aarhus C, Denmark
[g] Institut für Materialphysik, Universität Wien, A-1090 Wien, Austria

ARTICLE INFO

Article history:
Available online 20 January 2009

PACS:
68.43.Fg
61.14.Hg
68.37.Ef

Keywords:
Rhodium
Surface X-ray diffraction (SXRD)
In situ
Single crystal surfaces
Surface structure

ABSTRACT

Using a combination of experimental and theoretical techniques, we show that a thin RhO_2 surface oxide film forms prior to the bulk Rh_2O_3 corundum oxide on all close-packed single crystal Rh surfaces. Based on previous reports, we argue that the RhO_2 surface oxide also forms on vicinal Rh surfaces as well as on Rh nanoparticles. The detailed structure of this film was previously determined using UHV based techniques and density functional theory. In the present paper, we also examine the structure of the bulk Rh_2O_3 corundum oxide using surface X-ray diffraction. Being armed with this structural information, we have explored the CO oxidation reaction over Rh(1 1 1), Rh(1 0 0) and $Pt_{25}Rh_{75}$(1 0 0) at realistic pressures using *in situ* surface X-ray diffraction and online mass spectrometry. In all three cases we find that an increase of the CO_2 production coincides with the formation of the thin RhO_2 surface oxide film. In the case of $Pt_{25}Rh_{75}$(1 0 0), our measurements demonstrate that the formation of bulk Rh_2O_3 corundum oxide poisons the reaction, and argue that this is also valid for all other Rh surfaces. Our study implies that the CO oxidation reaction over Rh surfaces at realistic conditions is insensitive to the exact Rh substrate orientation, but is rather governed by the formation of a specific surface oxide phase.

1. Introduction

Heterogeneous catalysis forms the basis for much of modern chemistry and consequently the interaction between various molecules and metal surfaces has been thoroughly studied. While such studies on low-index single crystal surfaces in ultra high vacuum (UHV) have provided a detailed understanding of catalytic reactions under such conditions [1,2], the relevance of this knowledge to industrial catalysis is in many cases questionable. Increasing attention is therefore directed at studies of industrially more relevant systems involving higher gas pressures and/or more complex surfaces [3,4].

Due to its simplicity in combination with its direct relevance to industry, the most studied reaction, in this context, is the oxidation of CO. This reaction is efficiently catalyzed by late transition metals, such as Rh, Pt and Pd, where the major role of the catalyst is to dissociate the O_2 molecules, which happens spontaneously in the adsorption process. Once free oxygen atoms are present on the surface, CO adsorbing there can react with this O and desorb as CO_2. Since oxidation of metal surfaces has been found to block the CO oxidation, it has been generally accepted that the active phase of these catalysts is the metallic surface.

Another metal commonly used for catalyzing CO oxidation is Ru. Compared to the metals mentioned above, Ru is a rather poor catalyst under UHV compatible conditions, but superior at high pressures. This was explained about a decade ago by Over et al., who showed that the RuO_2(1 1 0) surface exposes special sites where the CO can adsorb and react with O in the oxide structure [5,6]. Similar behavior has been found for Rh, Pt and Pd as well, where the CO oxidation reactivity increases dramatically with the formation of a thin oxide film on the catalyst surface [7–13]. Thus, although still under debate [14,15], it is increasingly realized that oxygen dissociation induced *oxidic* phases plays an important role in the promotion of the catalytic activity of these materials. Further, the exact role of the oxides in the reaction process is not known on the atomic scale during the reaction at realistic pressures, resulting in an active scientific debate [16–18].

In this paper we summarize our results on the structure and reactivity of Rh oxides on pure Rh as well as PtRh alloy surfaces. On these surfaces, the oxidation process is similar, with the formation

* Corresponding author.
E-mail address: edvin.lundgren@sljus.lu.se (E. Lundgren).

0920-5861/$ – see front matter © 2008 Elsevier B.V. All rights reserved.
doi:10.1016/j.cattod.2008.11.011

of an ultra-thin Rh surface oxide at intermediate O_2 pressures, which develops into a corundum structured Rh_2O_3 bulk oxide at sufficiently high pressures. The reactivity of these oxides has been studied by *in situ* surface X-ray diffraction (SXRD) and mass spectrometry. Due to the weak interaction between X-rays and gases, SXRD is well suited for studying gas–surface interactions at atmospheric ambient pressures [19]. Our studies at these pressures, but still using single crystals as model systems, connect to our studies using traditional electron based surface science techniques, so that a detected phase can easily be determined during the reaction and related to the catalytic activity. In all cases, our studies show that while the bulk Rh oxide is inactive, the formation of a thin surface oxide coincides with a dramatic increase in the reactivity.

2. Experiment

The SXRD measurements were performed in the high pressure chamber [20] at the surface diffraction beamline ID3 [21] of the European Synchrotron Radiation Facility (ESRF) in Grenoble, France. The wavelength of the incident X-rays was set to 0.724 Å. The sample was aligned according to the bulk Bragg reflections of the Rh substrates. The coordinates (H, K, L) in reciprocal space refer to a basis $(\mathbf{b}_1, \mathbf{b}_2, \mathbf{b}_3)$ with $\mathbf{b}_1$ and $\mathbf{b}_2$ spanning the surface lattice of the Rh substrate, as shown in Fig. 1 a and b for (1 1 1) and (1 0 0), respectively, and $\mathbf{b}_3$ being perpendicular to the surface plane.

The high resolution core level spectroscopy (HRCLS) and low energy electron diffraction (LEED) measurements were performed at beamline I311 at MAX II in Lund, Sweden [22] using normal emission of the photoelectrons. The measurements were done at liquid nitrogen temperatures in order to reduce thermal broadening. The scanning tunneling microscopy (STM) measurements were done in two different experimental chambers, one in Vienna at room temperature using the same instrument as in Ref. [23], and one in Lund using the same instrument as in Refs. [24,25].

The CO oxidation measurements were performed in a batch reactor allowing for *in situ* SXRD measurements [20,26], in which the system is first stabilized in the presence of pure O_2. CO is then introduced into the chamber and the oxidation reaction starts. As one O_2 molecule can oxidize two CO molecules and the CO partial pressure is kept below twice that of O_2, the O_2/CO pressure ratio is automatically increased as the reaction proceeds, creating a more oxidizing environment. The partial gas pressures, the surface phase and the sample temperature can be followed with time during the reaction. In the end of the experiment, we can retrieve the starting conditions by evacuating the gas from the chamber and refill it with O_2. The CO gas line is specially equipped with a piece of curled copper tubing, which can be heated to 575 K and acts as a trap for Ni carbonyls. The line also has two liquid N_2 traps to further clean the CO by subsequent steps of condensation and distillation [26].

We follow the product formation (CO_2) via online mass spectrometry during the CO oxidation. By leaking the gas mixture from the batch reactor into the differentially pumped mass spectrometry chamber, the gas composition was monitored online. The response of the mass spectrometer to a change of the gas composition in the reaction cell is < 5 s.

The crystals were cleaned as in Ref. [27]. The sample temperature was measured using a tungsten–rhenium thermocouple (type C), mechanically clamped between the ceramic heating plate and the tantalum sample clips. Also here Ni was avoided in order to eliminate the risk of Ni carbonyl contamination.

3. Results

3.1. Surface oxide formation

In this section, we first describe the surface oxide previously found on all close-packed surfaces. After that we illustrate how the structural details of the surface oxide can be obtained by using a combined experimental and theoretical approach.

The interaction between Rh single crystals and low pressures of O_2 has been thoroughly studied and results in a range of different chemisorbed structures [28,29], but is out of topic for the present paper. At an oxygen pressure of between 10^{-5} and 10^{-3} mbar, depending on the surface density, the oxidation process starts with the formation of a surface oxide. This structure, exhibiting a close-packed trilayer of O–Rh–O as shown in Fig. 2, was first determined for Rh(1 1 1) using a multimethod approach combining density functional theory (DFT), LEED, HRCLS, STM, and SXRD as reported in Ref. [23]. The in-plane unit cell size of the surface oxide is found to be $a_{so} = 3.02$ Å, which on top of the substrate lattice with $a_{Rh(1\,1\,1)} = 2.69$ Å results in a coincidence lattice between (8×8) oxide cells and (9×9) substrate cells. Later, similar structures have been found on Rh(1 0 0) [27] and Rh(1 1 0) [30] as well. In the latter cases, the oxide adapts to the substrate, forming $c(8 \times 2)$ and $c(4 \times 2)$ superstructures, respectively. In contrast to the (1 1 1) case, this results in slightly distorted hexagonal oxide lattices with in-plane lattice constants of 3.07 and 3.09 Å for Rh(1 0 0) and 3.08 and 3.12 Å for Rh(1 1 0). A number of surface oxides has recently been found on other late transition metals [31].

Fig. 3 shows LEED, STM, SXRD and HRCLS results from the surface oxide as found on Rh(1 1 1). The moiré pattern found in LEED is straightforward to interpret as resulting from the coincidence between the surface oxide and substrate lattices. This interpretation

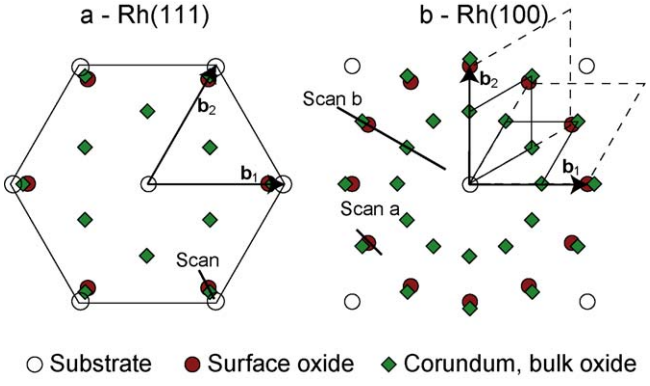

Fig. 1. Map of the reciprocal lattice of Rh(1 1 1) and Rh(1 0 0) including the surface oxide as well as the corundum Rh_2O_3 structures. The line marked 'Scan' in panel (a) indicates the SXRD scan used in the reactivity measurements for Rh(1 1 1) shown in Fig. 8. In panel (b), 'Scan a' and 'Scan b' correspond to the SXRD scans used in the reactivity measurements for $Pt_{25}Rh_{75}$(1 0 0) shown in Fig. 9 a and b, respectively.

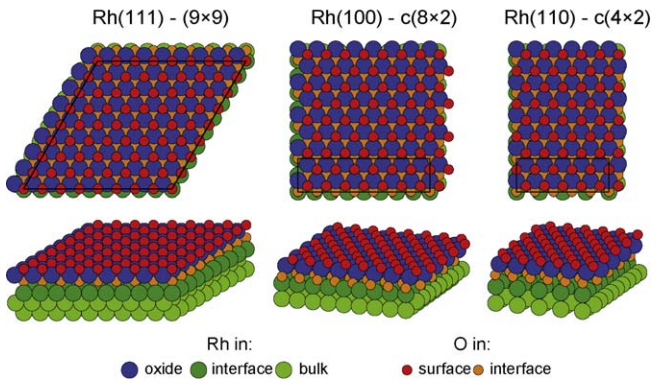

Fig. 2. Models of the surface oxide structure as found on Rh(1 1 1), Rh(1 0 0) and Rh(1 1 0).

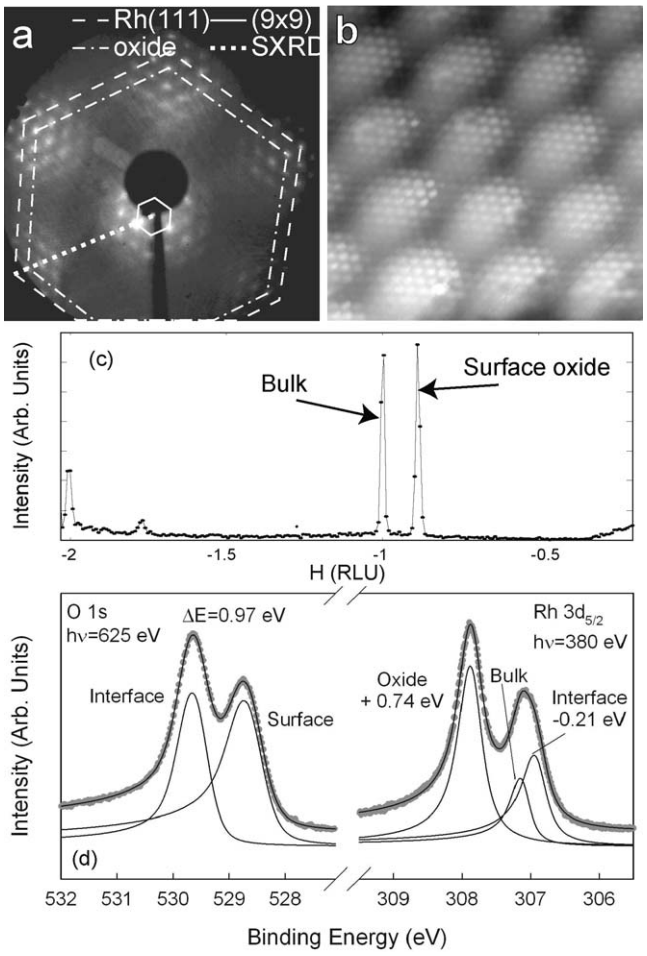

Fig. 3. (a) LEED, (b) STM, (c) SXRD and (d) HRCLS results from the (9×9) surface oxide on Rh(1 1 1). The surface oxide consists of a hexagonal O–Rh–O trilayer, with an in-plane lattice constant $a_{ox} = (9/8)a_{Rh}$. This results in a coincidence between (8×8) oxide cells and (9×9) substrate cells, yielding a moiré pattern clearly visible in LEED and STM. (c) The SXRD in-plane scan in the direction of the dotted line in the LEED image, reveals an in-plane lattice constant for the surface oxide to be 3.02 Å. (d) The O 1*s* spectrum reveals two components corresponding to the two O layers in the oxide structure, while the Rh $3d_{5/2}$ spectrum reveals three component corresponding to the bulk, the Rh atoms in the surface oxide (+0.74 eV) and the atoms at the interface between the substrate and the oxide (−0.21 eV).

is confirmed by the STM image showing a long-range corrugation corresponding to the coincidence, and atomic resolution of the surface of the moiré structure [23]. While it is difficult to extract the exact periodicity from the LEED and STM images, SXRD can be used to probe the in-plane lattice constant with a high degree of precision. Fig. 3 c shows a SXRD in-plane scan in the direction of the dotted line in the LEED image at $L = 0.3$ RLU (reciprocal lattice units). The first and second order substrate crystal truncation rods (CTRs) are found at $H = -1$ and $H = -2$ RLU, respectively. In addition, peaks corresponding to the surface oxide show up at $H = -0.89$ and $H = -1.78$ RLU, yielding an in-plane lattice constant for the surface oxide of $a_{so} = (1/0.89)a_{Rh(1\,1\,1)} = (9/8)a_{Rh(1\,1\,1)} = 3.02$ Å, and a coincidence between (8×8) oxide cells and (9×9) substrate cells as discussed above.

Information about the chemical composition can be obtained from HRCLS results as shown in Fig. 3 d. The surface oxide is identified by the splitting of the O 1*s* spectrum into two peaks showing that two different kinds of O are present. The intensities of these peaks are close to equal, but by varying the photon energy the component at higher binding energy is found to be more 'bulk like' than the one at lower binding energies. This agrees well with two layers of oxygen in a lattice as described above. The Rh 3 $d_{5/2}$ spectrum reveals three peaks interpreted as corresponding to bulk, the interface between the substrate and the oxide, and the atoms within the surface oxide (see Fig. 2). The latter peak is shifted towards higher binding energies due to the high coordination to O atoms for Rh atoms in-between the two O layers. Further, the intensity of the surface oxide peak is close to that of the surface peak for a clean surface in agreement with the model showing one layer of Rh in-between two similar layers of O.

Having the experimental information above, it is possible to create a plausible model for the structure and perform *ab initio* calculations. First, the termination of a bulk corundum Rh_2O_3(0 0 0 1) surface was calculated. The calculations showed that Rh segregates from the second to the first Rh layer, yielding a termination of [bulk Rh_2O_3]–Rh–O_3–Rh_3–O_3, indicating a high stability of the Rh–O–Rh surface trilayer, consisting of close-packed O and Rh layers. Relaxing the top 3 layers on the Rh(1 1 1) surface resulted in an in-plane lattice constant of 3.10 Å, in good agreement with that measured by SXRD. Further confirmation of the structure could then be obtained by simulating the STM images and calculating the core level binding energy shifts [23]. A similar procedure was done for the surface oxide on the Rh(1 0 0) surface, the difference being that quantitative LEED and SXRD was also applied, firmly establishing the correct structure of the surface oxide [27]. In passing, we note that the STM images of the trilayer oxides on all Rh surfaces show point defects, probably oxygen vacancies, with typical concentrations of a few percent. To conclude, we have obtained 'fingerprints' for several different methods, in order to identify the surface oxide on single crystal surfaces in UHV as well as more complex substrates and surroundings when approaching realistic conditions.

3.1.1. Vicinal surfaces and nanoparticles

Having established that an O–Rh–O trilayer surface oxide is formed on all close-packed Rh surfaces, we turn our attention to

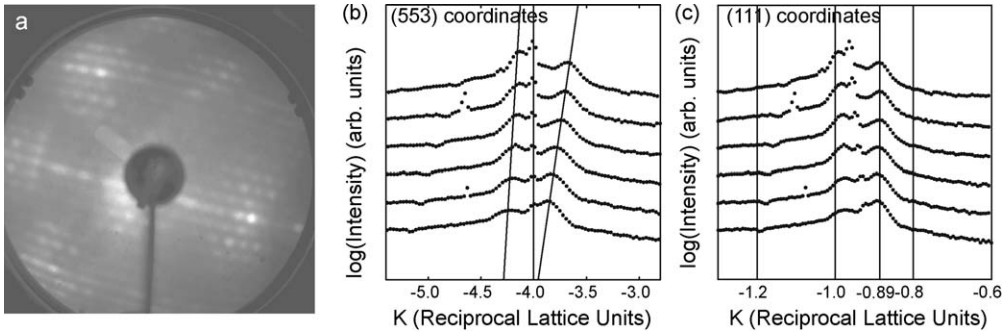

Fig. 4. LEED and SXRD measurements of oxidized Rh(5 5 3) showing that at 10^{-3} mbar the steps bunch together forming large surface (1 1 1) facets covered by the (9×9) surface oxide.

vicinal Rh surfaces and Rh nanoparticles. On vicinal Rh surfaces, oxygen exposure is found to induce large rearrangements of the surface [32–34]. Fig. 4 shows LEED and SXRD results after exposing a Rh(5 5 3) surface to 10^{-3} mbar of O_2 at 450 °C. The LEED pattern in panel (a) is similar, though less sharp, to the one from Rh(1 1 1) shown in Fig. 3 a. This indicates that the surface oxide is formed here as well but slightly less well ordered. The SXRD scans in Fig. 4 b and c are similar to the ones in Fig. 3 c, but in the *K* direction instead of *H*. Furthermore, they are made at several different *L* values and plotted in (5 5 3) and (1 1 1) coordinates in panels (b) and (c), respectively. Starting with panel (b), the peak at $K = -4$ RLU corresponds to the periodicity of the (5 5 3) planes. Since the other two peaks are moving when the *L* value is changed, they must origin from facets of a different surface orientation. By plotting the same scans in (1 1 1) coordinates instead, we see that the middle peak is now moving while the other two are constant in *K*. As in the case of the (1 1 1) surface (Fig. 3c), the peaks are found at $K = -1$ and $K = -0.89$ RLU, corresponding to the in-plane periodicity of the (1 1 1) substrate planes and the surface oxide, respectively. Hence the surface oxide is formed also on this vicinal surface and in order to fit the large unit cell of the (9×9) structure (seen in LEED) onto the (1 1 1) terraces, the surface is rearranged into large (1 1 1) and (1 1 $\bar{1}$) facets through step bunching. Similar results have been found for Rh(3 3 2) [33], which exposes (1 1 1) terraces separated by (1 0 0) steps, and this behavior seems to be general for vicinal Rh surfaces.

Turning to Rh nanoparticles, already a decade ago Rupprechter et al. observed the formation of a thin oxide layer on Rh particles by the use of transmission electron microscopy [35]. A thin Rh oxide phase was also found to be a highly effective catalyst using *in situ* X-ray absorption fine structure measurements [36]. A recent DFT study by Mittendorfer et al. shows that nanoparticles are expected to behave as the vicinal surfaces under oxygen exposure, hence exposing large (1 1 1) and (1 0 0) facets under pressures where the surface oxide is formed [37]. This was confirmed in a recent SXRD study by Stierle and co-workers [38]. Given this evidence, we conclude that the same surface oxide found on the close-packed single crystal surfaces as well as on vicinals, also forms on the facets of Rh nanoparticles.

3.1.2. Alloys: $Pt_{25}Rh_{75}$(1 0 0)

Turning to the oxidation of PtRh alloys in Fig. 5 we show HRCLS measurements of the Rh $3d_{5/2}$ and Pt 4 $f_{7/2}$ from the clean (bottom) and the oxygen exposed (top) $Pt_{25}Rh_{75}$(1 0 0) surface. For the clean surface, the Rh 3 $d_{5/2}$ level shows a weak surface component while the Pt 4 $f_{7/2}$ exhibits a strong surface component. These observations are consistent with Pt segregating to the surface under UHV conditions [39,40]. If the surface is exposed to 10^{-3} mbar O_2 at a sample temperature of 400 °C, the surface properties change significantly. In the Rh $3d_{5/2}$ level, a strong oxide component and a weak interface component appears, indicating that a surface oxide has formed. The binding energies of these components are close to those found for the surface oxide formed on the Rh(1 0 0) surface [27]. No oxide component can be observed in the Pt 4 $f_{7/2}$ level. The intensity relations are consistent with Rh segregating to the surface and forming a surface oxide while the interface between the surface oxide and the $Pt_{25}Rh_{75}$(1 0 0) is dominated by Pt, as illustrated in Fig. 5 b. In Fig. 5 c we show STM images from a $Pt_{25}Rh_{75}$(1 0 0) surface exposed to 10^{-4} mbar O_2 at a sample temperature of 400 °C. In this case the trilayer surface oxide has not completely covered the surface, but co-exists with the lower-coverage shifted row reconstruction [41]. The hexagonal nature of the surface oxide can clearly be seen, as well as a number of defects, presumably missing O atoms in the top-most O layer. Finally, the observed LEED pattern from the $Pt_{25}Rh_{75}$(1 0 0) oxidized surface is almost identical to that

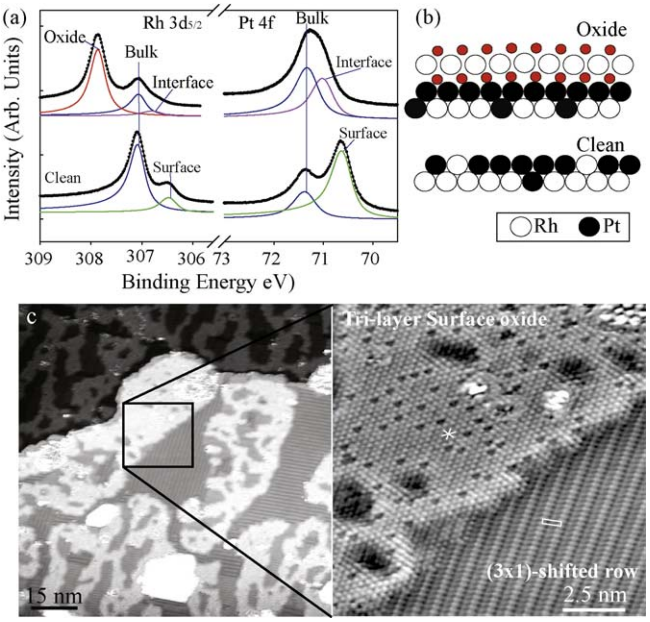

Fig. 5. (a) HRCLS from the clean and oxygen exposed $Pt_{25}Rh_{75}$(1 0 0) surface. The bottom Rh $3d_{5/2}$ and Pt 4 $f_{7/2}$ spectra from the clean surface both show well resolved surface components. The upper spectra show that while no oxide component can be observed in the Pt4f component after an O_2 exposure of 10^{-3} mbar at 400 °C, the Rh emission exhibits a clear oxide induced peak, similar to what has been observed previously on the Rh(1 0 0) surface [27]. (b) Models based on the HRCLS for the clean and the O exposed surface. (c) STM images (−1 V 0.65 nA) from a $Pt_{25}Rh_{75}$(1 0 0) surface exposed to 10^{-4} mbar O at a sample temperature of 400 °C. The brighter areas correspond to the trilayer surface oxide while the darker to the *p* (3×1)structure.

observed from the Rh(1 0 0) surface [27], the difference being weaker coincidence spots and the higher partial pressure needed for the full surface oxide formation on $Pt_{25}Rh_{75}$(1 0 0). All in all, our results are in good agreement with previous observations of the segregation of Pt and Rh in the presence of oxygen [41], and that at higher oxygen exposures the trilayer O–Rh–O surface oxide is formed on the alloy surface as well.

3.2. Bulk oxidation

At significantly higher oxygen pressures a thicker bulk-like oxide film is formed [23], which displays a corundum structure as shown in Fig. 6. The cell is built up by 6 units, each containing two slightly separated hexagonal Rh layers, with one atom each, and a single three times denser O layer, yielding a stoichiometry of Rh_2O_3. The structure has a lattice constant of 5.13 Å in the plane, and 13.8(= 6×2.3)Å out of the plane.

The corresponding reciprocal lattice will have an in-plane lattice constant of $2.69/5.13 = 0.544$ RLU_{111} (reciprocal lattice units relative to the Rh(1 1 1) lattice), which if rotated 30° relative to the Rh(1 1 1) lattice yields a reciprocal lattice map as described by the squares in Fig. 1. Note especially the $(H, K) = (-1, -1)$ CTR appearing at $(-0.907, 0)$ RLU_{111}, only slightly outside the $(-1, 0)$ reflection of the surface oxide. Out of the plane the reciprocal lattice constant will be $6.58/13.8 = 0.477$ RLU_{111}. Due to the internal structure of the unit cell, however, some of the lattice points will be absent or have a low intensity in the SXRD measurements. The distance of 2.3 Å between adjacent Rh layers results in pronounced peaks at a distance of 2.86 RLU_{111} along the CTRs.

In order to describe the expected intensities as measured by SXRD, the individual structure factor of each lattice point has to be calculated. These are shown in Fig. 7 a–d, where the area of each

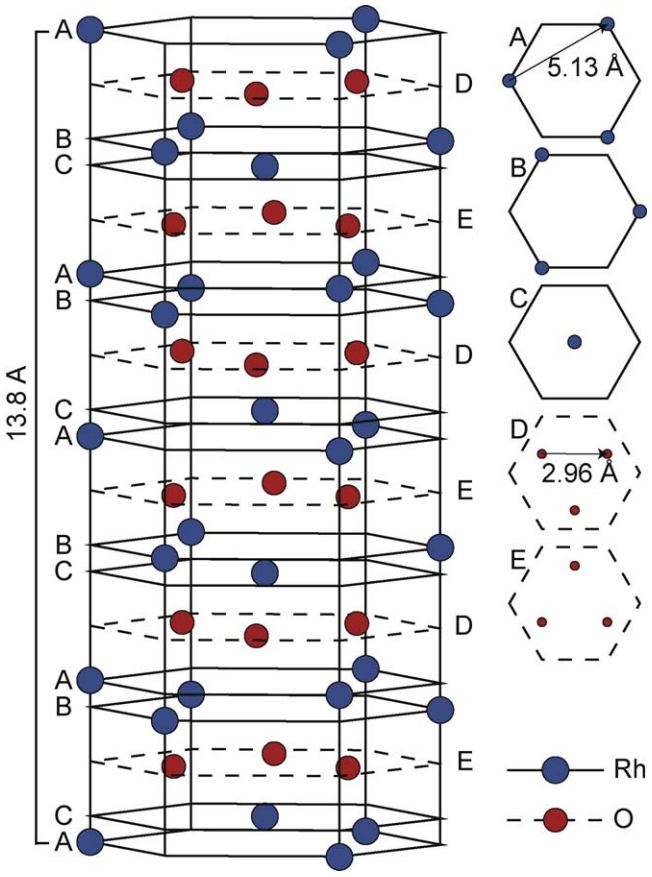

Fig. 6. Model of the Rh_2O_3 bulk oxide corundum structure.

point reflects the magnitude of the structure factor. In the figure, the structure factors along each CTR (H, K) is superimposed by the corresponding $(-H, -K)$ in order to account for the expected presence of two different domain orientations (rotated 180° with respect to each other).

After exposing the Rh(1 1 1) surface to 100 mbar of oxygen at 650 °C, a well-ordered bulk oxide of this structure could be found with SXRD. The sample was then cooled and the UHV chamber evacuated. This procedure did not affect the oxide within our detection limits. *L*-scans along a number of CTRs from the oxide reflections were recorded, as shown in Fig. 7 e–l. The peak positions and intensities should be compared to the corresponding structure factors as shown in Fig. 7 a–d, where the spot sizes are proportional to the strengths of the individual structure factors. All the experimental scans are well reproduced by the calculations, proving that this oxide has the Rh_2O_3 corundum structure.

3.3. Catalytic activity—metal, surface oxide, and bulk oxide

The catalytic activity towards CO oxidation was studied in a batch reactor, which was first filled with O_2 followed by pulses of CO. The activity is measured by mass spectrometry following the decrease in O_2 and CO and increase in CO_2 partial pressures. Simultaneously the phase of the model catalyst is monitored by *in situ* SXRD.

In pure O_2, as discussed above, a Rh oxide is formed, either in the form of a surface oxide, a bulk oxide or a mixed phase with surface-oxide and bulk-oxide covered areas. When CO is introduced the reaction starts consuming oxygen from the oxides to form CO_2. Depending on the amount of CO that is introduced, the oxides can be either partly or completely reduced. As will be shown below, the reactivity is very high when the surface oxide is present, but low otherwise, i.e. both in the metallic and the bulk oxidized phase. As the reaction proceeds, since each O_2 molecule consumes

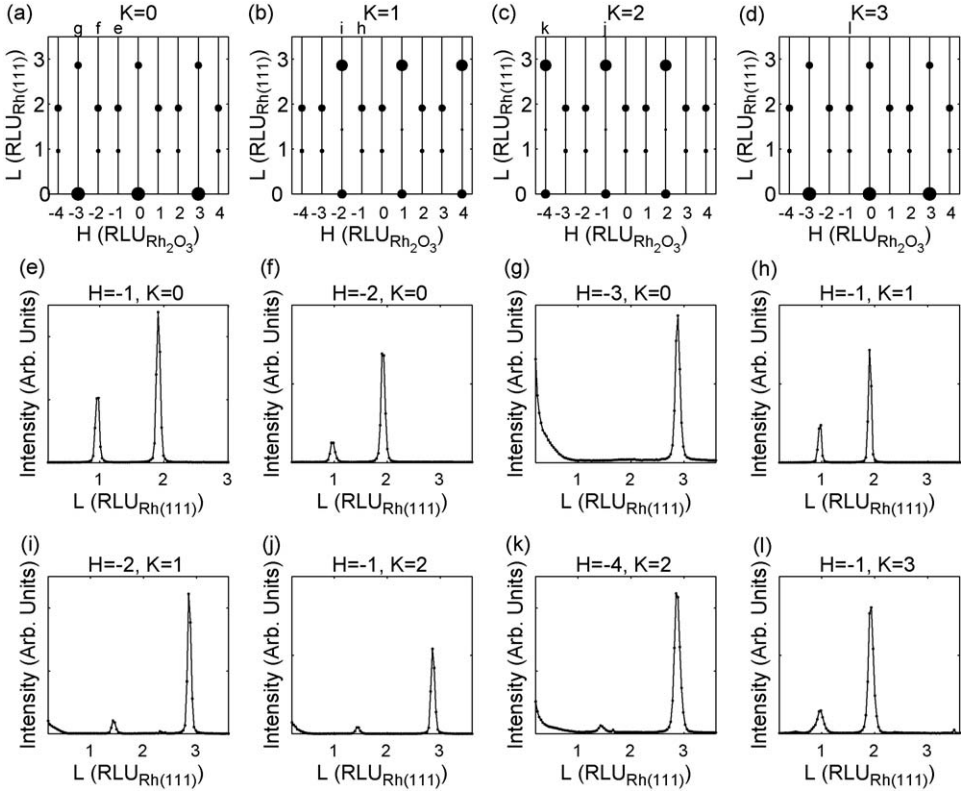

Fig. 7. (a–d) Calculated positions and structure factors for reflections corresponding to the Rh_2O_3 corundum structure. (e–l) Measured CTRs from a Rh(1 1 1) surface exposed to 100 mbar of O at 650° C showing excellent agreement with the calculations, confirming that the oxide formed exhibits the corundum structure.

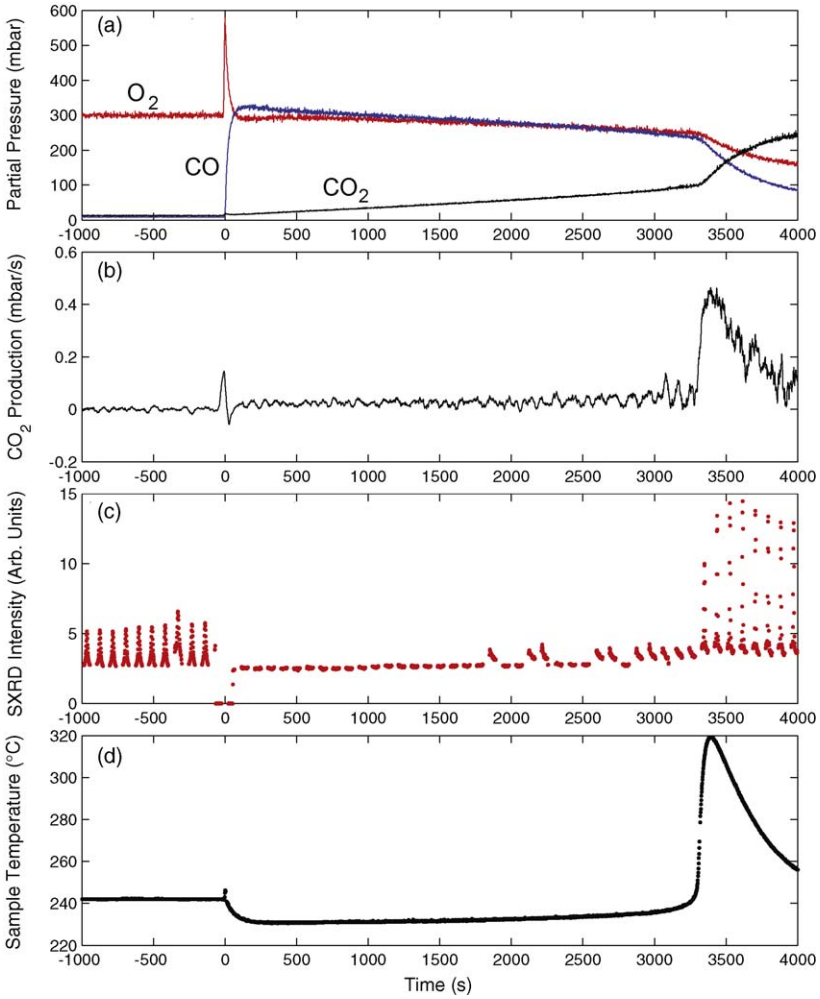

Fig. 8. The CO oxidation and surface structure of the Rh(1 1 1) surface during the reaction. (a) Partial pressures of O_2, CO and CO_2. The experiments starts in pure O_2, and CO is added at $t = 0$, which starts the CO oxidation reaction. As the reaction proceeds the O_2 and CO pressures decreases, while the CO_2 signal is rising. At $t \approx 3300$ s, there is a sudden increase in the reaction speed, as is directly monitored in (b). (b) The CO_2 production as derived from (a). Frame (c) shows consecutive SXRD scans along the line 'Scan' in Fig. 1a, showing the presence or absence of the surface oxide. The surface oxide is removed immediately after adding the CO at $t = 0$, and reappears simultaneously with the dramatic increase of the reaction rate at $t \approx 3300$ s. (d) Sample temperature during the experiment. Notice, the dramatic increase in sample temperature simultaneous with the switch to high activity.

two CO molecules, the O_2/CO partial pressure ratio increases, and at one point the gas mixture again becomes oxidizing enough for the surface oxide to return. Simultaneously we find that the high activity returns.

3.3.1. Pure Rh

Fig. 8 shows the results of such an experiment on Rh(1 1 1). Panel (a) shows the mass spectrometry signals corresponding to O_2, CO and CO_2. The chamber is initially filled with 300 mbar O_2 and at $t = 0$, the same amount of CO is introduced, starting the CO oxidation reaction. The reaction rate can be followed directly in the derivative of the CO_2 signal as shown in panel (b). Panel (c) shows the SXRD surface oxide signal as measured by consecutive scans along the line marked 'Scan' in Fig. 1 a. Finally, the sample temperature is monitored in panel (d).

Concentrating first on the reactivity as shown in Fig. 8 b, we find a sharp peak at $t = 0$, followed by a low activity until $t \approx 3300$ s, where the activity suddenly rises by about one order of magnitude. Continuing to panel (c), in pure oxygen ($t < 0$) we find that the surface oxide is present. SXRD data around $t = 0$ is missing since we, with the present setup, cannot do SXRD measurements while manually changing the gas pressures. It is clear, however, that the introduction of CO eventually reduces the surface oxide. Here, the surface is catalytically highly reactive for some time, probably until the surface oxide disappears and does not form again, explaining the peak in reactivity at $t = 0$. The surface is now found in a metallic phase in which it is presumably covered by CO until $t \approx 3300$ s, where the surface oxide returns. Note that the switch between metallic and oxidized phase coincides perfectly with the rise in reactivity.

The sample temperature shown in Fig. 8 d tells a similar story; starting at a preset temperature of 240 °C, there is a small peak as the surface oxide is reduced at $t = 0$, followed by a slight decrease of the temperature due to the larger cooling effect of the higher gas pressure now present in the chamber. After the switching to high activity at $t \approx 3300$ s, the CO oxidation reaction heats the sample and the temperature rises as much as 80 °C. It could be argued that sample temperature governs the formation of the surface oxide, and thus the formation of the surface oxide is due to the increased reaction rate heating the sample, although we have no indications for this. However, whatever the reason for the appearance of the surface oxide, reactivity increases strongly as soon as it appears. Furthermore, at the highest reactivity, the rate is probably limited by CO diffusion in the gas phase. The reaction rate is so fast that the nearby volume around the sample becomes depleted by CO, and therefore the reaction rate becomes saturated. This means that if

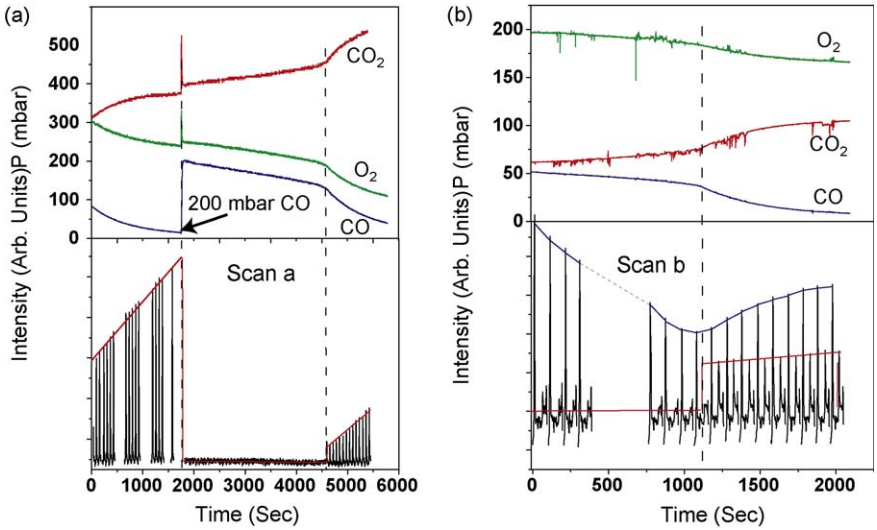

Fig. 9. (a) CO oxidation on $Pt_{25}Rh_{75}$(1 0 0). Repetitive HK-scans ('Scan a' in Fig. 1b; $L = 0.5$) during reaction conditions (bottom part) with simultaneous mass spectroscopy measurements of the gas content (top part). The red intensity envelope indicates the surface oxide diffraction peak. (b) Repetitive HK-scans ('Scan b' indicated in Fig. 1b) during reaction conditions (bottom part) with simultaneous mass spectroscopy measurements of the gas content (top part). The blue and red intensity envelopes indicate the bulk and the surface oxide diffraction peaks, respectively. (For interpretation of the references to color in this figure legend, the reader is referred to the web version of the article.)

no CO diffusion limit would have existed, the observed reaction rate would have been even higher. Future experiments using a flow reactor with smaller volume and by the use of smaller samples should reduce experimental problems due to temperatures and diffusion limitations.

At first glance, one might get the impression that the surface oxide actually poisons the surface, since the CO production rate eventually decreases after the appearance of the surface oxide. However, the following simple argumentation shows that the decrease in reactivity can be explained by the consumption of the CO and the declining sample temperature. Assuming an Arrhenius-like temperature dependence of the reactivity with a barrier of 0.51 eV [10], a temperature drop from 320 to 260 ◦ C would yield an activity decrease by a factor of 3. Adding to this that the CO pressure decreases from 250 to 100 mbar would in total result in a 7.6 times lower activity. The peak activity in Fig. 8 b is close to 0.45 mbar/s and as a result we would expect an activity of 0.059 mbar/s at the end of the experiment. This agrees nicely with our experimental results, where we find a CO_2 production rate between, between 0.05 and 0.1 mbar/s at the end of the experiment, in good agreement with the above estimation. Thus, the decline in activity can be explained by the decline in temperature and CO pressure alone, and is therefore not connected to a poisoning of the surface by the surface oxide.

From these measurements it is clear that the appearance of the surface oxide dramatically increases the catalytic reactivity of the Rh(1 1 1) model catalyst. As reported in Ref. [11], very similar results were found for Rh(1 0 0), indicating that the substrate surface orientation is of minor importance and the catalytic activity is instead controlled by the surface oxide formation. Since this process is found to be similar on all Rh surfaces, including those of nanoparticles, these results can be expected to be valid also for industrial catalysts.

3.3.2. $Pt_{25}Rh_{75}$(1 0 0)

Similar measurements on the $Pt_{25}Rh_{75}$(1 0 0) alloy surface are shown in Fig. 9. In panel (a), the SXRD scans, shown in the lower part, were preformed along the line in Fig. 1 b marked 'Scan a'. In this experiment the PtRh surface was initially exposed to 500 mbar O_2 at 500 K, and a number of CO pulses, inducing reduction and reoxidation, were supplied. At $t = 0$, the surface oxide peak can clearly be observed. By introducing 200 mbar CO ($t \approx 1750$ s), the surface oxide is removed as evidenced by the disappearance of the diffraction peak. At $t \approx 4600$ s, the O_2/CO pressure ratio is high enough for the trilayer surface oxide to return and, as in the case of pure Rh, this coincides with a dramatic increase of the CO oxidation rate.

In Fig. 9 b, the SXRD scans are performed along 'Scan b' indicated in Fig. 1 b, and monitor the presence of the surface oxide as well as bulk oxide. In this experiment the sample was initially exposed to 250 mbar of O_2 at 500 K, resulting in a mixed phase with surface oxide as well as bulk oxide present. Introducing 61 mbar of CO (not shown) removed the surface oxide film while the bulk oxide remained, co-existing with metallic surface areas. This is the situation found at $t = 0$. At $t \approx 1125$ s, the O_2/CO pressure ratio is again high enough for the surface oxide to reappear, which as above coincides with a large increase in reactivity. This experiment shows that while the surface oxide film is essential for the increase of the catalytic reactivity, the bulk oxide film rather poisons the surface, in accordance with earlier observations [42]. The fact that the surface oxide film is active in CO oxidation but not the bulk oxide was recently confirmed by the use of low energy electron microscopy (LEEM) [43].

4. Discussion

We have shown that in the case of Rh as well as PtRh alloy single crystals, the same trilayer O–Rh–O surface oxide is formed. Furthermore, ample evidence in the literature indicates that the same thin oxide is also formed on Rh nanoparticles [35,37,38]. This is a remarkable observation, and demonstrates the stability and ubiquitousness of this particular surface oxide.

In the case of Pd, the situation is different. Here, a large number of different surface oxides can be formed [24,25,44–49] prior to the bulk PdO formation [50,51] depending on surface orientation and terrace width. Concerning the reactivity, the active phase of Pd has been attributed to a thin PdO film [8] as well as an ordered surface oxide in CO oxidation [12], and in the case of methane oxidation PdO seeds [52].

Returning to Rh, the reactivity data in the present manuscript shows that, at relevant pressures and temperatures, the catalytic activity for CO oxidation is drastically increased with the formation

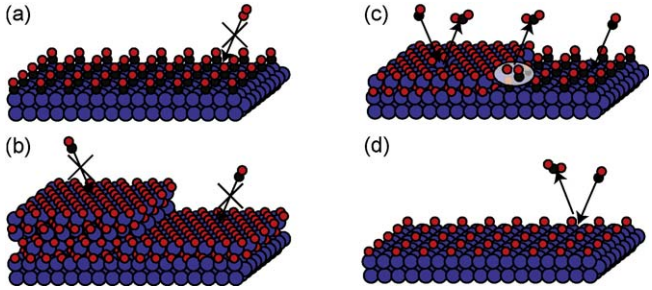

Fig. 10. Different phases in which the catalyst surface can be found in an atmosphere of O_2 and CO. If the surface is CO covered (a), there is not enough space left in order to allow for dissociative O_2 adsorption and the reactivity is low. (b) Perfect films of the surface or bulk oxides blocks the CO adsorption and hence the catalytic activity. Co-existence of CO covered metallic surface and surface oxide (c) allows O and CO to react along the edges of the surface oxide. Finally, an oxygen covered metallic surface (d) allows CO adsorption and is active. The latter surface has not, however, been observed *in situ* under industrially relevant conditions, and as mentioned above the reaction barriers are expected to be higher in this case than in (c).

of the trilayer. This is clear from the *in situ* measurements presented above.

Under UHV conditions, the fact that CO has a very low adsorption energy on the surface oxide [53], would imply the opposite, namely that the surface oxide poisons the surface. In order to find an explanation for the behavior at elevated pressures, Fig. 10 shows a number of different phases, in which the catalyst surface can be found. Our model is based on previous UHV observations [53] and DFT calculations [10]. In panel (a) the surface is in a metallic phase covered by adsorbed CO molecules. Since the O_2 adsorption is dissociative it needs a larger free surface area than can be found in-between the CO molecules, which makes this phase inactive. Similarly, the oxide surfaces shown in panel (b) are fully covered by O atoms which does not allow for CO adsorption, also resulting in inactive surfaces. To make the surface oxide active, either defects or co-existing metallic areas, where the CO can adsorb, are needed (panel (c)). Alternatively a surface with adsorbed O atoms, as shown in panel (d), will still allow for CO adsorption (which is not dissociative) and be active. According to the DFT calculations in Ref. [10], however, the reaction barriers involved in forming CO_2 using chemisorbed O is significantly higher than those for using O from the edge of the surface oxide, and hence the reactivity is expected to be lower in case (d) as compared to (c). A border type of process is also supported by our previous UHV based investigations of the reduction of the trilayer on Rh(1 1 1) [53]. In that study, we could show that the reduction starts at defects, and expands in a circular fashion from the initial reduction seed.

However, it could be argued that a different phase and/or a different process could be responsible for the increased activity, and that the surface oxide would not participate in the reaction. In this scenario, the surface oxide would be a mere byproduct of having surface areas where O_2 dissociation is still possible, but with the CO oxidation occuring in this other surface phase. For example, our measurements cannot exclude the presence of a disordered chemisorbed oxygen or disordered surface oxide [54,55] phase on the surface, although we have never observed such a phase previously either *ex situ* in UHV [56] or during *in situ* studies at higher pressures. As SXRD is not particularly sensitive to the oxygen atoms, we could also consider a different process based on a defective trilayer structure, in which oxygen vacancies or groups thereof in the top-most layer are the active sites at which CO can adsorb as proposed in Fig. 10(c). This could be described as a Mars–Van Krevelen type of process [57]. One reason for such a scenario could be the interfacial stress/strain between the trilayer and the Rh(1 1 1) surface as has recently been suggested [43], and would also explain the apparent inactivity of the thicker bulk oxide although its surface structure appears to be the same as the structure of the trilayer. On the other hand, the inactivity of the bulk oxide could also be explained if the trilayer of the bulk oxide is too high above the substrate so that the CO can not reach it at the borders, or that the bulk oxide trilayer has no O vacancies for chemical reasons.

5. Conclusions

In summary, we have investigated the details of the oxidation of Rh at realistic oxygen pressures. Thin RhO_2 surface oxide films form prior to the bulk Rh_2O_3 corundum oxide on all Rh surfaces investigated so far. This includes Rh vicinal surfaces and Rh nanoparticles. Furthermore, by the use of *in situ* surface X-ray diffraction combined with online mass spectrometry, we have shown that the presence of a trilayer RhO_2 surface oxide always coincides with a high CO_2 production rate, suggesting that the trilayer oxide is highly active in CO oxidation. The formation of the bulk Rh_2O_3 oxide poisons the surface. Various reaction mechanisms for the observed behavior have been discussed.

Acknowledgements

This work was financially supported by the Swedish Research Council, the Austrian FWF, the Crafoord Foundation, the Anna and Edwin Berger Foundation, and the Knut and Alice Wallenberg Foundation. Support by the MAX-lab and ESRF staffs is gratefully acknowledged. The University of St Andrews is a charity registered in Scotland: No. SC013532.

References

[1] Introduction to Surface Chemistry and Catalysis, Wiley, New York, 1994.
[2] G. Ertl, H. Knözinger, J. Weitkamp, Handbook of Heterogeneous Catalysis, Wiley, New York, 1997.
[3] E. Lundgren, H. Over, J. Phys. Condens. Matter 20 (2008) 180302.
[4] A. Stierle, A. Moelenbroek, MRS Bull. 32 (2007) 1000.
[5] H. Over, Y.D. Kim, A.P. Seitsonen, S. Wendt, E. Lundgren, M. Schmid, P. Varga, A. Morgante, G. Ertl, Science 287 (2000) 1474.
[6] J. Assmann, D. Crihan, M. Knapp, E. Lundgren, E. Löffler, M. Muhler, V. Narkhede, H. Over, M. Schmid, A. Seitsonen, P. Varga, Angew. Chem. Int. Ed. 44 (2005) 917.
[7] B.L.M. Hendriksen, J.W.M. Frenken, Phys. Rev. Lett. 89 (2002) 046101.
[8] B.L.M. Hendriksen, S.C. Bobaru, J.W.M. Frenken, Surf. Sci. 552 (2004) 229.
[9] M.D. Ackermann, T.M. Pedersen, B.L.M. Hendriksen, O. Robach, S.C. Bobaru, I. Popa, C. Quiros, H. Kim, B. Hammer, S. Ferrer, J.W.M. Frenken, Phys. Rev. Lett. 95 (2005) 255505.
[10] R. Westerström, J.G. Wang, M. Ackermann, J. Gustafson, A. Resta, A. Mikkelsen, J.N. Andersen, E. Lundgren, O. Balmes, X. Torrelles, J.W.M. Frenken, B. Hammer, J. Phys. Condens. Matter 20 (2008) 184018.
[11] J. Gustafson, R. Westerström, A. Mikkelsen, X. Torrelles, O. Balmes, J.N. Andersen, C.J. Baddeley, E. Lundgren, Phys. Rev. B 78 (2008) 045423.
[12] J. Rogal, K. Reuter, M. Scheffler, Phys. Rev. B 75 (2007) 205433.
[13] F. Gao, M. Lundwall, D.W. Goodman, J. Phys. Chem. C 112 (2008) 6057.
[14] G. Rupprechter, C. Weilach, Nano Today 2 (2007) 20.
[15] F. Gao, S.M. McClure, Y. Cai, K.K. Gath, Y. Wang, M.S. Chen, Q.L. Guo, D.W. Goodman, Surf. Sci. (in press).
[16] M.S. Chen, Y. Cai, Z. Yan, K.K. Gath, S. Axnanda, D.W. Goodman, Surf. Sci. 601 (2007) 5326.
[17] H. Over, M. Muhler, A.P. Seitsonen, Surf. Sci. 601 (2007) 5659.
[18] H. Over, O. Balmes, E. Lundgren, Catal. Today (in press).
[19] S. Ferrer, M.D. Ackermann, E. Lundgren, MRS Bull. 32 (2007) 1010.
[20] P. Bernard, K. Peters, J. Alvarez, S. Ferrer, Rev. Sci. Instrum. 70 (1999) 1478.
[21] S. Ferrer, F. Comin, Rev. Sci. Instrum. 66 (1995) 1674.
[22] R. Nyholm, J.N. Andersen, U. Johansson, B.N. Jensen, I. Lindau, Nucl. Instrum. Methods Phys. Res. A 467–468 (2001) 520.
[23] J. Gustafson, A. Mikkelsen, M. Borg, E. Lundgren, L. Köhler, G. Kresse, M. Schmid, P. Varga, X. Yuhara, C. Torrelles, J.N. Quirós, Andersen, Phys. Rev. Lett. 92 (2004) 126102.
[24] M. Todorova, E. Lundgren, V. Blum, A. Mikkelsen, S. Gray, J. Gustafson, M. Borg, J. Rogal, K. Reuter, J.N. Andersen, M. Scheffler, Surf. Sci. 541 (2003) 101.
[25] P. Kostelník, N. Seriani, G. Kresse, A. Mikkelsen, E. Lundgren, V. Blum, T. Šikola, P. Varga, M. Schmid, Surf. Sci. 601 (2007) 1574.
[26] M.D. Ackermann, Ph.D. Thesis, Kamerlingh Onnes Laboratory, Leiden University, Leiden, The Netherlands, 2007.

[27] J. Gustafson, A. Mikkelsen, M. Borg, J.N. Andersen, E. Lundgren, C. Klein, W. Hofer, M. Schmid, P. Varga, L. Köhler, G. Kresse, N. Kasper, A. Stierle, H. Dosch, Phys. Rev. B 71 (2005) 115442.
[28] M.V. Ganduglia-Pirovano, M. Scheffler, A. Baraldi, S. Lizzit, G. Comelli, G. Paolucci, R. Rosei, Phys. Rev. B 63 (2001) 205415.
[29] A. Baraldi, J. Phys. Condens. Matter 20 (2008) 093001, and references therein.
[30] C. Dri, C. Africh, F. Esch, G. Comelli, O. Dubay, L. Köhler, F. Mittendorfer, G. Kresse, P. Dudin, M. Kiskinova, J. Chem. Phys. 125 (2006) 94701.
[31] E. Lundgren, A. Mikkelsen, J.N. Andersen, G. Kresse, M. Schmid, P. Varga, J. Phys. Condens. Matter 18 (2006) 481.
[32] J. Gustafson, A. Resta, A. Mikkelsen, R. Westerström, J.N. Andersen, E. Lundgren, J. Weissenrieder, M. Schmid, P. Varga, N. Kasper, X. Torrelles, S. Ferrer, F. Mittendorfer, G. Kresse, Phys. Rev. B 74 (2006) 35401.
[33] J. Klikovits, Ph.D. Thesis, TU Wien, 2008 (unpublished).
[34] J. Klikovits, M. Schmid, L.R. Merte, P. Varga, R. Westerström, A. Resta, J.N. Andersen, J. Gustafson, A. Mikkelsen, E. Lundgren, F. Mittendorfer, G. Kresse, Phys. Rev. Lett. 101 (2008) 266104.
[35] G. Rupprechter, K. Hayek, H. Hofmeistery, J. Catal. 173 (1998) 409.
[36] M.A. Newton, A.J. Dent, S. Diaz-Moreno, S.G. Fiddy, B. Jyoti, J. Evans, Chem. Eur. J. 12 (2006) 1975.
[37] F. Mittendorfer, N. Seriani, O. Dubay, G. Kresse, Phys. Rev. B 76 (2007) 233413.
[38] P. Nolte, A. Stierle, N.Y. Jin-Phillipp, N. Kasper, T.U. Schulli, H. Dosch, Science 321 (2008) 1654.
[39] E. Platzgummer, M. Sporn, R. Koller, S. Forsthuber, M. Schmid, W. Hofer, P. Varga, Surf. Sci. 419 (1999) 236.
[40] E.L.D. Hebenstreit, W. Hebenstreit, M. Schmid, P. Varga, Surf. Sci. 441 (1999) 441.
[41] M. Sporn, E. Platzgummer, E.L.D. Gruber, M. Schmid, W. Hofer, P. Varga, Surf. Sci. 416 (1998) 384.
[42] C.H.F. Peden, D.W. Goodman, D.S. Blair, P.J. Berlowitz, G.B. Fischer, S.H. Oh, J. Phys. Chem. 92 (1988) 1563.
[43] J.I. Flege, P. Sutter, Phys. Rev. B 78 (2008) 153402.
[44] E. Lundgren, G. Kresse, C. Klein, M. Borg, J.N. Andersen, M. De Santis, Y. Gauthier, C. Konvicka, M. Schmid, P. Varga, Phys. Rev. Lett. 88 (2002) 246103.
[45] G. Zheng, E.I. Altman, J. Phys. Chem. B 106 (2002) 1048.
[46] R. Westerström, J. Gustafson, A. Resta, A. Mikkelsen, J.N. Andersen, E. Lundgren, N. Seriani, F. Mittendorfer, M. Schmid, J. Klikovits, P. Varga, M.D. Ackermann, J.W. Frenken, N. Kasper, A. Stierle, Phys. Rev. B 76 (2007) 155410.
[47] J. Klikovits, E. Napetschnig, M. Schmid, N. Seriani, O. Dubay, G. Kresse, P. Varga, Phys. Rev. B 76 (2007) 045405.
[48] R. Westerström, C.J. Weststrate, A. Resta, A. Mikkelsen, J. Schnadt, J.N. Andersen, E. Lundgren, M. Schmid, N. Seriani, J. Harl, F. Mittendorfer, G. Kresse, Surf. Sci. 602 (2008) 2440.
[49] H.H. Kana, J.F. Weaver, Surf. Sci. 602 (2008) 53.
[50] E. Lundgren, J. Gustafson, A. Mikkelsen, J.N. Andersen, A. Stierle, H. Dosch, M. Todorova, J. Rogal, K. Reuter, M. Scheffler, Phys. Rev. Lett. 92 (2004) 046101.
[51] G. Ketteler, D.F. Ogletree, H. Bluhm, H.J. Liu, E.L.D. Hebenstreit, M. Salmeron, J. Am. Chem. Soc. 127 (2005) 18269.
[52] H. Gabasch, K. Hayek, B. Klötzer, W. Unterberger, E. Kleimenov, D. Teschner, S. Zafeiratos, M. Ha1vecker, A. Knop-Gericke, R. Schlögl, B. Aszalos-Kiss, D. Zemlyanov, J. Phys. Chem. C 111 (2007) 7957.
[53] E. Lundgren, J. Gustafson, A. Resta, J. Weissenrieder, A. Mikkelsen, J.N. Andersen, L. Köhler, G. Kresse, J. Klikovits, A. Biederman, M. Schmid, P. Varga, J. Electron Spectrosc. Relat. Phen. 144 (2005) 367.
[54] G.L. Kellogg, Surf. Sci. 171 (1986) 359.
[55] Medvedev, et al. Langmuir 14 (1998) 6151.
[56] L. Köhler, G. Kresse, M. Schmid, E. Lundgren, J. Gustafson, A. Mikkelsen, M. Borg, J. Yuhara, J.N. Andersen, M. Marsman, P. Varga, Phys. Rev. Lett. 93 (2004) 266103.
[57] P. Mars, D.W. van Krevelen, Spec. Suppl. Chem. Eng. Sci. 3 (1954) 41.